Free-electron vortices in photoelectron momentum distributions from molecules with coupled electronic-nuclear motion

Paul Winter and Manfred Lein*
Leibniz University Hannover, Institute of Theoretical Physics, Appelstr. 2, 30167 Hannover, Germany
(Dated: May 22, 2026)

Counter-rotating circularly polarized, time-delayed pulses generate electron wave packets that interfere in momentum space and form spiral-shaped free-electron vortices. By numerically solving the non-Born-Oppenheimer time-dependent Schrödinger equation for one-photon single ionization of H_2, we show that these spirals rotate within the polarization plane as a function of the nuclear energy. A kinematical model, based on the instantaneous sharing of photon energy between the freed electron and the parent molecular ion, predicts this rotation and agrees quantitatively with the simulations. We further demonstrate that integrating over vibrational energies diminishes the visibility of the interference structure. Results from fixed-nuclei and atom-like reference calculations resemble single vibrational channels, whereas incoherent summation over multiple vibrational states leads to blurring and noticeable shifts of the apparent rotation. The joint-energy spectrum exhibits pronounced electron-nuclear correlation lines. In the case of co-rotating pulses, these lines are related to the interference rings in the momentum distribution. Conversely, for counter-rotating pulses, they originate from a dipolar modulation of the spiral pattern, caused by the nonisotropic molecular orbital.

I. INTRODUCTION

Photoelectron momentum distributions (PMDs) are a sensitive probe of ionization dynamics, providing temporal information through streaking and attoclock-type measurements as well as structural information through light-induced electron diffraction and photoelectron holography [1–16]. Among the most striking interference patterns in PMDs are free-electron vortices (FEVs), observed when two counter-rotating circularly polarized attosecond pulses ionize the target with a controlled time delay [17, 18]. Each pulse launches an outgoing electron wave packet of the same electron with an angular-momentum character determined by the number of absorbed photons. Due to the delay, the two wave packets differ by a relative Ramsey-like phase and interfere at detection. For a co-rotating pulse sequence, the magnetic quantum numbers m of the outgoing wave packets are equal and concentric rings appear in the polarization plane. Counter-rotating pulses impose opposite angular-momentum changes and the interference give rise to spirals, with the number of spiral arms given by twice the number of absorbed photons when identical central frequencies are assumed [17]. The spiral winding is governed by the delay τ, with an energy spacing $\Delta E_{\mathrm{spiral}} = 2\pi/\tau$ between adjacent fringes in radial direction. FEVs have been demonstrated and analyzed across perturbative single- and multiphoton ionization, resonance-enhanced multiphoton ionization, and even above-threshold and tunneling regimes, both in atoms (H, He, K, Ar, Na) and molecules (H_2^+, H_2, CO_2, N_2, HF, Kr_2) [17–28]. They have been used to probe AC Stark effects, retrieve electronic phases, and access electron–electron correlations [21, 29–32].

A compact kinematical description of FEVs follows from first-order perturbation theory for single-photon ionization [17, 20]. The maxima of the interference fringes are approximately described by a Fermat spiral at the azimuth angle (atomic units are used throughout)

$$\varphi(p) = \phi_{\mathrm{rot}} - \frac{\tau p^2}{4} + \pi k\,, \tag{1}$$

with an overall rotation angle of

$$\phi_{\mathrm{rot}} = -\frac{\tau I_p + \phi_{12}}{2}\,, \tag{2}$$

where p is the electron momentum in the polarization plane, τ is the pulse delay, I_p is the ionization potential, $k \in \{0, 1\}$ counts the spiral arms and ϕ_{12} is the relative carrier–envelope phase, which, for the sake of simplicity, is assumed to be zero throughout this work. Equation (1) captures the geometric (kinematical) contribution governed by pulse timing and polarization, while Eq. (2) reflects the energy offset that sets the absolute angular orientation. Deviations from the purely kinematical picture, termed dynamical FEV, arise from target specific properties such as dipole transitions moments, orbital shapes, and multi-orbital contributions [20, 27].

The energetics of the ionization step constrain the accessible photoelectron momenta. In single-photon ionization of atoms, the dominant radius of the PMD is set by energy conservation

$$\hbar\omega = E_{\mathrm{el}} + I_p + U_p\,, \tag{3}$$

where $\hbar\omega$ is the photon energy, $E_{\mathrm{el}} = p^2/2$ is the electron kinetic energy, and $U_p = \mathcal{E}_0/(4\omega^2)$ the ponderomotive potential (often negligible for weak fields). In molecules, the photon energy can be shared between the photoelectron and the vibrational motion of the ion(s). Moreover, the

* lein@itp.uni-hannover.de

ionized molecule may fragment, i.e., we may have dissociative ionization. For a vertical transition in H_2 at an internuclear distance $R_{\rm ion}$,

$$\hbar\omega \approx E_{\rm el} + E_{\rm nuc} + V_D - E_{H_2} + U_p\,, \tag{4}$$

where $E_{\rm nuc}$ is the energy corresponding to the internuclear motion (vibrational binding energy or fragment kinetic energy), V_D is the electronic energy of the fragments ($H+H^+$), and E_{H_2} is the ground-state energy of H_2. The energy sharing influences both the radius and the angular orientation of the spiral pattern. The energies are illustrated in Fig. A1 of the appendix.

While many molecular FEV studies employ fixed-nuclei or adiabatic-nuclei approximations and report deformations of the spiral due to the shape of the contributing molecular orbitals [22, 25, 27, 33], semi-classical analyses suggest a measurable sensitivity to electron–nuclear coupling, non-adiabatic effects, and intermediate resonances [28]. Here we solve a non-Born-Oppenheimer (non-BO) time-dependent Schrödinger equation (TDSE) for aligned H_2 in the perturbative single-photon (two-armed FEV) regime to explicitly include coupled electron–nuclear dynamics. We show that the FEV rotates systematically with the nuclear energy for both vibrationally bound and dissociative channels. We also show that this rotation is quantitatively captured by the kinematical description, Eq. (1) and Eq. (2), once electron–nuclear energy sharing is accounted for through an appropriate molecular definition of the ionization potential. We further discuss experimental implications: integrating over nuclear energies, as in velocity-map imaging without coincidence resolution, reduces contrast and biases the rotation, whereas electron–ion coincidence measurements enable a clean observation. Finally, we demonstrate that the mapping between the spiral's radius and its rotation angle Eq. (1), combined with the nonisotropy of the molecular orbital, results in correlation lines with sub-photon spacing in the joint-energy spectrum (JES) for a counter-rotating pulse sequence. We compare our results with fixed-nuclei and atomic simulations and with a co-rotating pulse sequence.

II. NUMERICAL MODEL

In this section we describe a non-BO model with coupled electronic and nuclear motion optimized for the H_2 molecule. Details about the numerical parameters can be found in Appendix A.

In this study we focus on one-photon single ionization by two circularly polarized few-femtosecond pulses. To model this process, we need at least a two-dimensional description [$\vec{r} = (x, y)^T$] of the freed electron under the influence of the two-dimensional field polarization. We call it the active electron. The second ("inactive") electron of H_2 is assumed to stay always bound and is restricted to populate only the two lowest dipole-coupled energy levels ($j = 0, 1$) of H_2 ($X^1\Sigma_g^+$ and $B^1\Sigma_u^+$) and H_2^+ ($1s\sigma_g$ and $2p\sigma_u$) respectively. Considering at least two levels for the inactive electron enables us to capture effects such as bond-softening [34], bond-hardening [35], electron localization [36], and above-threshold dissociation [37, 38]. The motion of the nuclei is treated in a one-dimensional description with the internuclear coordinate R. We do not consider center-of-mass and rotational motion of the molecule. We align the molecule along the y axis with the nuclear center of mass at the origin of the active-electron coordinate system. This results in a two-level wave function depending on three spatial dimensions (2D electron + 1D nuclei),

$$\Psi(t) = \begin{pmatrix} \psi_0(\vec{r}, R, t) \\ \psi_1(\vec{r}, R, t) \end{pmatrix}\,. \tag{5}$$

The interaction between the molecular ion (both nuclei and the bound electron) and the active electron is modeled by soft-core interaction potentials depending on the inactive-electron state ($j = 0, 1$),

$$V_j^{\rm int}(\vec{r}, R) = \sum_{k=1,2} \frac{-Z_j^{\rm eff}(R, |\vec{r} - \vec{R}_k|)}{\sqrt{|\vec{r} - \vec{R}_k|^2 + \alpha_j(R)}}\,, \tag{6}$$

where $\vec{R}_k = \{-R/2\,\hat{e}_y, R/2\,\hat{e}_y\}$ are the positions of the nuclei, $R = |\vec{R}_1 - \vec{R}_2|$, $Z_j^{\rm eff}$ is an effective charge, and α_j is a softening parameter. The effective charge and the softening parameter are adjusted to numerically reproduce the ionization potential $\Delta V_j(R) = V_j^{\rm ion}(R) - V_j^{H_2}(R)$ for both electronic states of H_2 based on literature values of the potential curves [39–42]. In Appendix A we give more details on the optimization procedure and the resulting electronic structure of this model.

Within the inactive-electron state j, the Hamiltonian in dipole approximation governing the wave function $\psi_j(\vec{r}, R, t)$ is given by

$$H_j = \frac{\left[\vec{p} + \vec{A}(t)\right]^2}{2} + \frac{P^2}{2\mu} + V_j^{\rm ion}(R) + V_j^{\rm int}(\vec{r}, R)\,, \tag{7}$$

for $j = \{0, 1\}$, where $\vec{p}$ is the momentum of the active electron, $\vec{A}(t)$ the vector potential of the field, P the momentum of the nuclei, $\mu = m_{H^+}/2$ is the reduced mass of the nuclei with m_{H^+} the proton mass [43], and $V_j^{\rm ion}$ are the numerical potential curves of the molecular ion H_2^+ [39]. Note that the interaction potential vanishes for large distances of the active electron, $V_j^{\rm int}(\vec{r} \to \infty, R) = 0$. This decouples the Hamiltonian into the driven motion of the active electron and a two-level molecular ion with nuclear motion.

The inactive (bound) electron can be excited by the external field via an interaction potential

$$W = -\vec{d}(\vec{r}, R) \cdot \vec{\mathcal{E}}(t)\,, \tag{8}$$

with the electric field $\vec{\mathcal{E}}(t) = -\partial_t \vec{A}(t)$ and the transition dipole moment $\vec{d}$. Thus, the full Schrödinger equation

can be written as

$$\mathrm{i}\partial_t \begin{pmatrix}\psi_0\\ \psi_1\end{pmatrix} = \begin{pmatrix}H_0 & W\\ W & H_1\end{pmatrix}\begin{pmatrix}\psi_0\\ \psi_1\end{pmatrix}. \tag{9}$$

We solve the TDSE Eq. (9) on a Cartesian grid using a split-operator method (SOM) [44, 45] with a time step of $\Delta t \approx 0.054$ a.u. The freed electron may travel a large distance. To reduce the needed box sizes, we apply a two-grid method [46]. Outgoing electronic wave packets are projected onto Volkov states using a complex absorbing potential and then propagated in momentum space neglecting the interaction potential. The nuclear motion is treated similarly with a SOM, but the ion potential is always retained because the separation of the nuclei remains moderate. In the absorption step, zero-padding is applied to increase the resolution of the momentum of the freed electron and to enlarge the box size of the internuclear distance after ionization. We use a grid of 384 points for each electronic coordinate with $\Delta x = \Delta y = 0.4$ a.u. For the nuclei we use 256 points with $\Delta R = 0.05$ a.u. The enlarged (due to zero-padding) second grid has $1024^2 \times 512$ grid points. The simulations start in the ground state $\Psi(t=0) = \Psi_0 = (\psi_0(t=0), 0)^T$ obtained by imaginary-time propagation [47] followed by the real-time propagator eigenstate method [48]. We obtain a ground-state energy of $E_{\mathrm{H}_2} \approx -1.1645$ a.u. (-31.7 eV) consistent with values reported in [39, 49].

The vector field $\vec{A}(t)$ is defined as a sum of circularly polarized (CP) pulses,

$$\vec{A}_{R/L}(t) = -\frac{\mathcal{E}_0}{\omega} f(t) \begin{pmatrix}\cos(\omega t)\\ \pm\sin(\omega t)\end{pmatrix}, \tag{10}$$

with positive/right (R) or negative/left (L) helicity. Here, $\mathcal{E}_0$ is the maximal electric-field strength, ω is the frequency, and $f(t) = \cos^4\left(\frac{\omega t}{2N}\right)$ is an envelope function. We use the combinations

$$\vec{A}(t) = \begin{cases}\vec{A}_R(t) & \text{RCP},\\ \vec{A}_R(t) + \vec{A}_R(t-\tau) & \text{RRCP},\\ \vec{A}_L(t) + \vec{A}_R(t-\tau) & \text{LRCP},\end{cases} \tag{11}$$

with time delay τ. Only the left-right circularly polarized (LRCP) pulse creates FEVs. The right-right circularly polarized (RRCP) pulse is known to cause a ring structure in the PMD [17, 18]. We use a wavelength of $\lambda = 40$ nm, which corresponds to a photon energy of approximately 31 eV. The field strength is set to $\mathcal{E}_0 = 0.00533803$ a.u. ($I = \epsilon_0 c \mathcal{E}_0^2 \approx 2\,\frac{\mathrm{TW}}{\mathrm{cm}^2}$) and each pulse has a duration of $N = 8$ cycles (ca. 1 fs). In the following, we delay the two pulses by 12, 14, and 16 optical cycles ($\tau_1 \approx 1.6$ fs, $\tau_2 \approx 1.9$ fs, and $\tau_3 \approx 2.1$ fs), so the pulses are well separated.

After the end of the pulse sequence we project the outer-grid wave function onto vibrational bound and discretized continuum states $\chi_{j,v}$ of the nuclei,

$$\psi_j(\vec{p}, R) = \sum_{v\in\mathbb{N}_0} c_{j,v}(\vec{p})\chi_{j,v}(R) \tag{12}$$

$$\text{with} \quad c_{j,v}(\vec{p}) = \langle \chi_{j,v}(R) | \psi_j(\vec{p}, R)\rangle \tag{13}$$

with $\chi_{j,v}$ solving the one dimensional time-independent Schrödinger equation

$$\left[\frac{P^2}{2\mu} + V_j^{\mathrm{ion}}(R)\right]\chi_{j,v}(R) = E_{j,v}\chi_{j,v}(R), \tag{14}$$

with $E_{j,v}$ being the energy of the nuclei. The continuum states are approximated as the box states of the grid. We obtain $\chi_{j,v}$ by numerically exact diagonalization of the short-time propagator [48] of Eq. (14) to ensure stationary propagation without field. The energy of the nuclei is $E_{j,v}^{\mathrm{nuc}} = E_{j,v} - V_D$, with $V_D = V^{\mathrm{ion}}(R\to\infty) = -0.5$ a.u. This energy is positive for dissociated states and negative for vibrational bound states of H_2^+. The coefficients $c_{j,v}$ can be used to calculate the energy spectrum of the nuclei,

$$\frac{\mathrm{d}W_j(E_{j,v}^{\mathrm{nuc}})}{\mathrm{d}E} \approx \frac{\iint \mathrm{d}p_x \mathrm{d}p_y\, |c_{j,v}(\vec{p})|^2}{\Delta E_{j,v}}, \tag{15}$$

where $\Delta E_{j,v}$ is obtained from linear interpolation of the differences of the energies, $\delta E_{j,v} = E_{j,v+1} - E_{j,v}$. To calculate the PMD, we add the individual PMDs of both electronic states incoherently,

$$M(\vec{p}, E_{\mathrm{nuc}}) = M_0(\vec{p}, E_{\mathrm{nuc}}) + M_1(\vec{p}, E_{\mathrm{nuc}}), \tag{16}$$

with

$$M_j(\vec{p}, E_{\mathrm{nuc}}) = \sum_{v}^{E_{j,v}^{\mathrm{nuc}}\in I} |c_{j,v}(\vec{p})|^2. \tag{17}$$

The interval $I = [E_{\mathrm{nuc}} - \Delta E/2, E_{\mathrm{nuc}} + \Delta E/2]$ accounts for finite resolution in experiments, needed for sufficient yield. When not stated otherwise, we use an interval of $\Delta E = 0.1$ eV for dissociation. The discrete bound states for $j = 0$ can be added in Eq. (17) or analyzed individually. In the following we restrict our analysis to nuclear energies below 2.1 eV, where we found negligible contributions of the $2p\sigma_u$ ($j = 1$) state. In a coincidence measurement the direct single ionization into the electronic ground state of H_2^+ can be distinguished from other channels by selecting appropriate energies of the nuclei [50].

III. RESULTS

A. Rotation angle

We first report the results of our TDSE simulations for an LRCP pulse with a time delay of 12 cycles ($\tau_1 \approx$

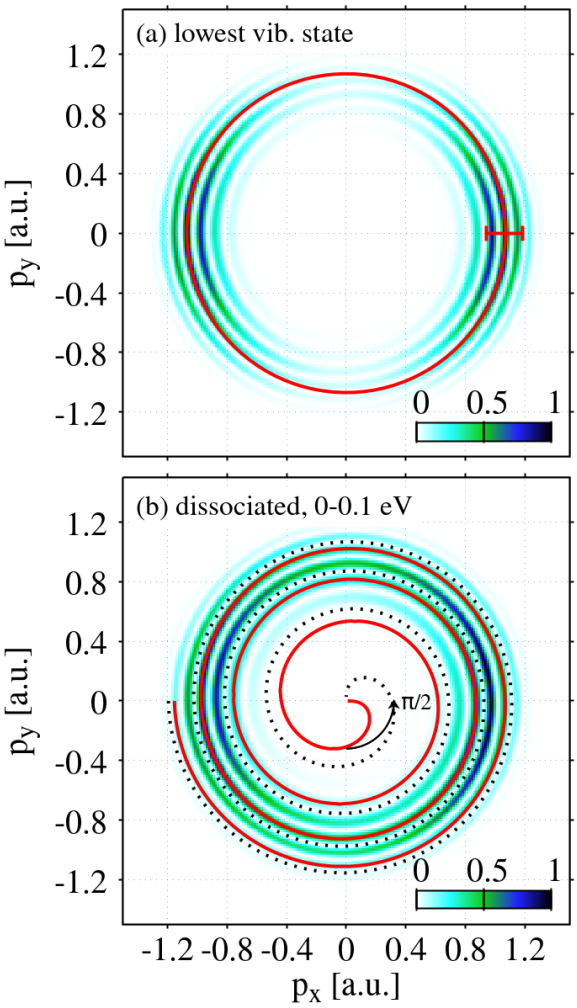

Figure 1. Photoelectron momentum distributions normalized to maximum value 1 for two different energy regions of the nuclei after ionization by an LRCP pulse with a time delay of 12 cycles ($\tau_1 \approx 1.6$ fs). (a) Lowest vibrational bound state of H_2^+ in $1s\sigma_g$ with energy $E_{0,v=0} \approx -0.5975$ a.u. The red circle shows the electron momentum $p_{\rm el} \approx 1.07$ a.u. according to energy conservation and the red horizontal line is the estimated width $\Delta p_{\rm width} = 0.25$ a.u. based on the frequency spectrum of a single pulse. (b) Integrated PMD for an energy region of $0 - 0.1$ eV for the nuclei. The red line represents a spiral arm from the kinematical model Eq. (1). The black dotted line is the spiral arm rotated by $\pi/2$.

1.6 fs). In Fig. 1, examples of photoelectron momentum distributions are given for different energy ranges of the nuclei. Figure 1(a) shows the PMD obtained for the H_2^+ photoion in the lowest vibrational state $v = 0$ of the $1s\sigma_g$ state ($j = 0$). The density is located along a ring with central radius $p_{\rm el} \approx 1.07$ a.u. (red circle), estimated by energy conservation $E_{\rm kin} = p_{\rm el}^2/2 = \hbar\omega - (E_{0,0} - E_{\rm H_2})$ with $E_{0,0}$ the energy of the ion. The width of the ring reflects the spectral width of the individual pulses. On top of the ring, there is a two-arm spiral interference structure overlaid with a dipolar modulation that has its maxima on the p_x axis. The pulse duration is short enough that multiple windings of the spiral are visible. The spiral structure, called FEV, is caused by the interference of time-delayed electronic wave packets originating from the two pulses in Eq. (11). The number of spiral arms confirms one-photon absorption [17, 18]. The pulse sequence ionizes the molecule with a probability of ca. 0.01% and the first excited electronic states of the inactive electron (inner and outer grid) are occupied with probability 0.001% at the end of the simulation, validating the perturbative character of the chosen parameters.

The dipolar pattern is a signature of the nonisotropic molecular orbital shape, which has the potential to deform the interference pattern. It appears also when using only a single pulse or in fixed-nuclei simulations, see Fig. 3(c). The strength of this modulation is related to the internuclear distance at the moment of ionization. An analysis of the integrand of the Franck-Condon factors $P_{\rm FC}(v) = \left|\int {\rm d}R\, \chi^*_{\rm H_2}(R)\chi_{0,v}(R)\right|^2$ representing the overlap of the vibrational state $\chi_{\rm H_2}$ of the neutral molecule with individual vibrational states $\chi_{0,v}$ of the ion, for the low-lying vibrational states of H_2^+, reveals that the peak of the spatial distribution shifts toward smaller internuclear distances as the vibrational energy ($E_{0,v}$) increases. This occurs because the H_2 vibrational state overlaps primarily with the inner turning points of the H_2^+ vibrational states. Consequently, the $v = 0$ state exhibits the most pronounced dipolar pattern in the resulting photoelectron momentum distribution. This trend persists for dissociated nuclei, as they originate from ionization events at internuclear distances $R_{\rm ion}$ small enough so that $V_0^{\rm ion}(R_{\rm ion}) > V_D$. This condition is satisfied for $R_{\rm ion} \le R_D$, where R_D is defined by $V_0^{\rm ion}(R_D) = V_D$.

In Fig. 1(b) we show a PMD for dissociated nuclei integrated in the energy range $[0, 0.1]$ eV, see Eq. (16). The dipolar modulation is weaker, which is consistent with ionization at small internuclear distances. In line with energy conservation, the radius is slightly reduced, because more energy is deposited into the nuclear motion. To guide the eye, we plot one arm of the two-armed spiral as a red line. This line is a kinematical description of the free electron vortices, see below, showing very good agreement with the TDSE result. The kinematical description is sufficient to reproduce the shape of the spiral, despite the dipolar pattern. A more precise prediction of the spiral shape is provided by perturbation theory [27].

The population of the bound and dissociated vibrational states after the end of the pulse is shown in the nuclear-energy spectrum Fig. 2(a). The spectrum follows qualitatively the distribution expected from Frank-Condon factors, although slightly shifted with a maximum at $v = 3$ instead of $v = 2$, and a less steep exponential decay into the dissociative region. This difference originates from a preferential ionization at smaller internuclear distances than the peak position of the H_2 vibrational ground state. We found a shift in the dominant position of ionization by $\Delta R_{\rm ion} \approx -0.046$ a.u. by ana-

lyzing the ionization yield for fixed nuclei. We also performed a two-level one-dimensional BO calculation with an initial nuclear wave packet peaked at $R = 1.4$ a.u. instead of the H_2 vibrational-ground-state peak position 1.45 a.u., which approximately reproduced the TDSE results in Fig. 2(a). The nuclear-energy spectrum is approximately identical for all considered time delays τ.

Assuming that dissociative ionization takes place most likely at very small radii $R_{\rm ion} \leq R_D$, nuclear motion starts on the repulsive part of the ion potential curve. This fraction, instantaneously created with zero initial velocity, is accelerated up to a kinetic energy of $E_{\rm nuc} = V_0^{\rm ion}(R_{\rm ion}) - V_D$. Instead of the atomic ionization potential I_p such as in Eq. (1), we introduce the molecular ionization potential $I_p(R) = V_0^{\rm ion}(R) - E_{\rm H_2}$ as the difference between the R-dependent ion potential curve and the initial energy of the neutral molecule. Inserting into Eq. (2), we end up with a rotation angle $\phi_{\rm rot}$ of the spiral depending on the energy of the nuclei,

$$\phi_{\rm rot}(E_{\rm nuc}) = -\frac{\tau(E_{\rm nuc} + V_D - E_{\rm H_2})}{2}\,. \qquad (18)$$

Thus, measuring the nuclei at increasing kinetic-energy releases is directly related to (i) a rotation and (ii) a shrinking of the radius of the spiral interference structure in the PMD. We use Eq. (18) also for bound states with $E_{\rm nuc} = E_{0,v} - V_D$.

To quantitatively compare the kinematical model with TDSE results, we extract by finding the local maxima $\varphi(p)$ along circles of varying radii. The numerical positions of these maxima (φ, p) are then fitted with the quadratic form $\varphi = a + bp^2$, see (1), to determine a and b. The results for the rotation angle are presented in Fig. 2(b) for three values of the time-delay τ. Where necessary, we added or subtracted multiples of π (similar to phase unwrapping). As expected from Eq. (18), we obtain a linear behavior. The spiral interference pattern rotates as a function of the nuclear energy. The model Eq. (18) and TDSE results agree very well within the numerical accuracy of the fitting process.

Next, we consider the PMD in coincidence measurements for the process $H_2 + \hbar\omega \to H_2^+ + e^-$, where vibrational states of H_2^+ cannot be resolved. For Fig. 3(b) we summed over all vibrational bound states of H_2^+. The general shape as well as the spiral interference structure is still visible, but significantly blurred [51]. We obtain a rotation angle of $\phi_{\rm rot} = 126.6°$, which is comparable to the 133.7° rotation angle of the dominant vibrational state ($v = 3$). The blurring of the PMD is caused by contributions from other vibrational states. As shown in Figure 2(b), the spiral rotates by more than 180° across the vibrational bound states, resulting in an interchange of the two spiral arms.

Because the frozen-nuclei approximation is widely used in attosecond strong-field ionization of molecules [27, 28, 33], we performed also a two-dimensional TDSE simulation with fixed internuclear distance $R = 1.4$ a.u. under the same physical conditions as our moving-nuclei model.

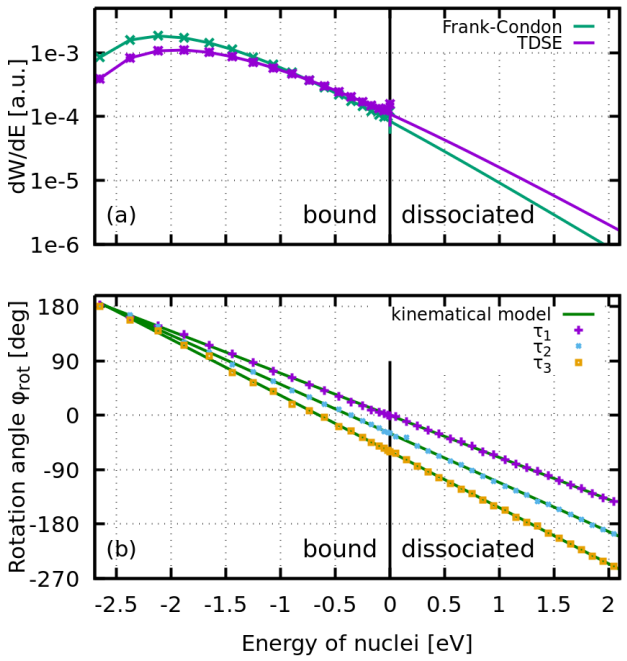

Figure 2. (a) Vibrational-energy distribution of the molecular ion at the end of the simulations in the σ_g state compared to the distribution expected from Franck-Condon factors (arbitrarily scaled for better comparison). (b) Rotation angle of FEVs extracted from the TDSE as a function of vibrational energy in comparison to a kinematical model based on instantaneous energy sharing, Eq. (18). At zero energy we find a rotation angle of ca. -0.08°, −30°, and −60° for $\tau_1 \approx 1.6$ fs, $\tau_2 \approx 1.9$ fs, and $\tau_3 \approx 2.1$ fs.

The resulting PMD is shown in Fig. 3(c). We find a much sharper pattern compared to the PMD summed over all vibrational states in Fig. 3(b). We obtain an extracted rotation angle of 116.6°, which is in good agreement with the kinematical model prediction of 113.6° using the corresponding $I_p = \Delta V_0(R) = V_0^{\rm ion}(R) - V_0^{\rm H_2}(R)$ in Eq. (2). The vibrational state $v = 4$ in the moving-nuclei calculation is energetically closest to the fixed-nuclei ionization. For $v = 4$ we have a rotation angle of 117.8° in Fig. 2(b) with a model prediction of 115.3°, which matches the fixed-nuclei simulation. In other words, the adiabatic ionization potential $I_p^{\rm adi} = E_{0,4} - E_{\rm H_2}$ is close to the vertical ionization potential of the fixed-nuclei calculation, leading to similar spirals, see Fig. 3(a),(c).

Last, in Fig. 3(d) we show a result of a 2D TDSE simulation for a model atom matching the ionization potential of the fixed-nuclei calculation. We used a soft-core potential $-1/\sqrt{|\vec{r}|^2 + \alpha_{\rm atom}}$ with $\alpha_{\rm atom} = 0.334$ and obtain a rotation angle of 116.4° consistent with the fixed-nuclei results. The major difference is the absence of the dipolar pattern, confirming that this pattern originates from the initial orbital shape of the electron.

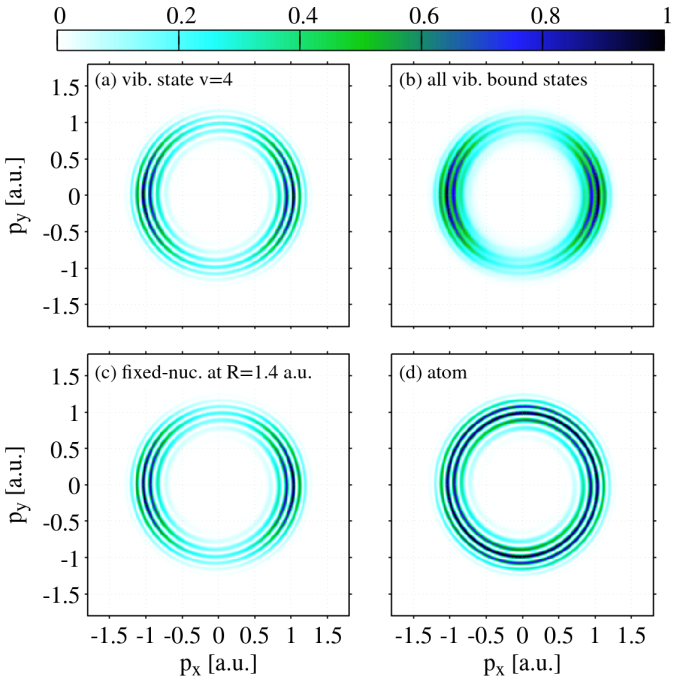

Figure 3. Normalized photoelectron momentum distribution correlated with (a) the vibrational bound state $v = 4$ of H_2^+, (b) summed PMD of all vibrational bound states, (c) result of a 2D fixed-nuclei TDSE simulation at an internuclear distant of $R = 1.4$ a.u., and (d) the 2D TDSE result for a model atom. All PMDs are obtained with an LRCP pulse and a time delay of 12 cycles ($\tau_1 \approx 1.6$ fs).

We conclude that the visual impression of the PMD for summed vibrational states is dominated by only a few bound states of H_2^+, while the other states cause to a significant blurring and a small shift in rotation angle compared to the dominant state. The fixed-nuclei and the model-atom simulations match very well the spiral from a single vibrational state with similar I_p. This shows that frozen-nuclei simulations can be indeed helpful, but experimental results might be notably different when multiple vibrational states are involved. The kinematical model, extended to instantaneous energy sharing at the moment of ionization, reproduces the numerical rotation angles of the FEVs very well.

B. Contrast

This section addresses the limitations caused by integration over nuclear energy ranges. In Fig. 4(a), we compare normalized cuts along the positive p_x axis of the PMDs shown in Fig. 3(a)–(c). While the positions of the maxima and minima agree well, the contrast of the oscillation differs. For better comparison, we define the

Table I. Contrast values C for distributions as in Fig. 4(a).

state	C
lowest vib. state $v = 0$	0.997
dominant vib. state $v = 3$	0.9992
highest vib. state $v = 18$	0.990
fixed nuclei	0.9998
summed over all bound states	0.48

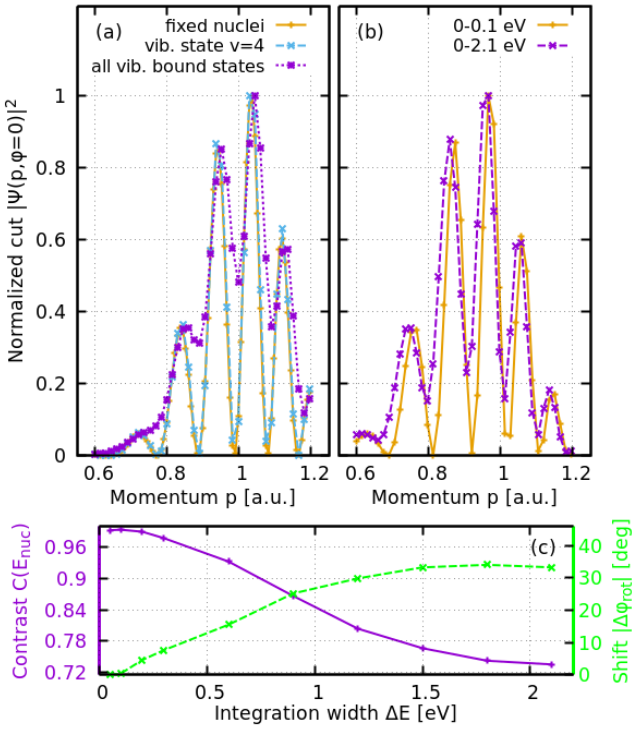

Figure 4. Analysis of the contrast in PMDs. Cuts of PMDs along the positive p_x axis: (a) Comparison of vibrational state $v = 4$, fixed-nuclei results, and the integrated PMD of all vibrational bound states of H_2^+. (b) Comparison of small and large integration regions of energies for the dissociation channel. (c) Contrast (purple line, left y axis) and relative shift of the rotation angle with respect to a small integration region (green dashed line, right y axis) as a function of the right boundary of the integration range for dissociation. Results are obtained for $\tau_1 \approx 1.6$ fs.

contrast

$$C = \frac{|\psi|^2_{\max} - |\psi|^2_{\min}}{|\psi|^2_{\max} + |\psi|^2_{\min}}, \tag{19}$$

where $|\psi|^2_{\max}$ is the global maximum of the cut and $|\psi|^2_{\min}$ is the smaller of the values at the minima neighboring the global maximum. Table I underlines the visual impression of Fig. 4(a) that the summed vibrational states has worse contrast compared to individual energies and also in comparison to the fixed-nuclei simulation. For the dissociation channel, the blurring effect is studied in

Figs. 4(b) and (c). First, we compare the cuts of PMDs for two different integration regions. The narrow integration region, covering a KER of $0-0.1\,\mathrm{eV}$, exhibits a high contrast and a well-defined rotation angle that remains essentially unchanged even when the integration window is further reduced. The large integration region from $0-2.1\,\mathrm{eV}$ shows a strongly shifted rotation angle of ca. 33°. A systematic scan through integration ranges $[0, \Delta E]$ is shown in Fig. 4(c). The contrast (purple line, left y axis) systematically decreases when more energies are summed. The contrast starts for very small integration ranges at approximately 1, similar to a single vibrational bound state, but decreases for $\Delta E = 2.1$ eV to below 75%. For even larger integration intervals the contrast does not change anymore, because of the small signal at high energies, see Fig. 2(a). The shift of the rotation angle, $\Delta\phi_{\mathrm{rot}} = |\phi_{\mathrm{rot}}^{0-\Delta E} - \phi_{\mathrm{rot}}^{0-0.05\ \mathrm{eV}}|$, increases as a function of the integration range, see Fig. 4(c). While large integration regions are often preferred to improve the signal-to-noise ratio, they may inadvertently obscure the measurement of the precise spiral rotation angle.

C. Electron-nuclei correlations

In this section, we report on the joint-energy spectrum (JES) of the photoelectron energy and the nuclear energy for different pulse configurations.

Single ionization with an RCP pulse creates a ring-shaped PMD with the radius depending on the energy of the nuclei. This yields a broad distribution in the JES in Fig. 5(a) following the energy correlation line (red line) defined by energy conservation Eq. (4) with neglected U_p. The width along the electron energy axis corresponds to the spectral bandwidth of the laser pulse. The extension of the distribution along the nuclear energy axis results from the nonzero width of the initial H_2 vibrational ground-state wave function, yielding a range of nuclear energies that is only weakly sensitive to variations in the pulse parameters. Not shown in this figure is that this structure repeats for larger electron energies in a distance of one photon energy $\hbar\omega \approx 31$ eV with smaller signal (above-threshold ionization).

Adding a second, either left circularly or right circularly polarized pulse causes a Ramsey-like interference as discussed in [17, 18, 20]. In contrast to the single-pulse JES, we see on top of the broad distribution in Fig. 5(b) and (c) a variation of the yield with maxima following a slope of -1 and repeating with a spacing $\Delta E_{\mathrm{cor}} = \frac{2\pi}{\tau_1} = 2.58\,\mathrm{eV}$ (orange dashed lines). For co-rotating circularly polarized pulses (RRCP) in Fig. 5(c) these correlation lines can be easily understood by looking at PMDs for a fixed nuclear energy. The PMDs show multiple, concentric interference rings. Integrating along the angle at a radius with large signal, leads to a corresponding maximum in the JES. Our results show that the electron energy of these peaks shifts, according to energy conservation, linearly with the energy of the nuclei, giving rise to the structure of diagonal lines in the JES.

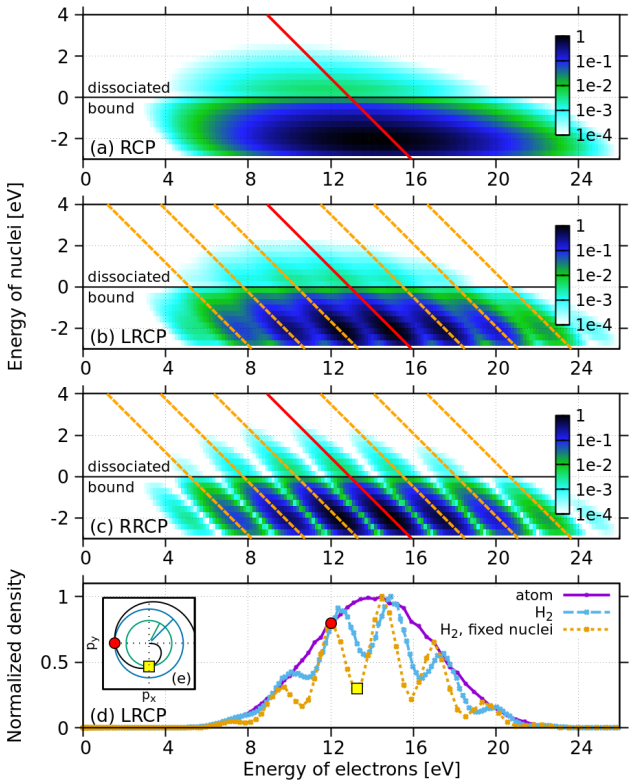

Figure 5. Normalized joint-energy spectrum of nuclei and photoelectrons for (a) a single RCP pulse, (b) an LRCP, and (c) an RRCP pulse sequence, showing correlation lines (red and orange lines) spaced by $\Delta E_{\mathrm{cor}} = \frac{2\pi}{\tau_1} = 2.58\,\mathrm{eV}$, which is much smaller than the photon energy ($\hbar\omega \approx 31\,\mathrm{eV}$). (d) Normalized electron-energy spectrum for an LRCP pulse. The magenta and dotted orange lines show the spectrum for the atom and the fixed-nuclei molecule with $R = 1.4\,\mathrm{a.u.}$, respectively. The dashed blue line shows the JES from (b) integrated over the nuclear energy. (e) Illustration of intersections of a spiral with circles of different radii. Yellow and red points mark intersections corresponding to minima and maxima in the electron energy spectrum, see main text. All distributions are normalized to the maximal value one.

For counter-rotating circularly polarized pulses (LRCP) in Fig. 5(b), the previous argumentation cannot be applied, because a spiral has no preferred radius. In this case the yield variation is caused by the dipolar pattern already discussed in Fig. 3(a)–(c) and Fig. 1. To illustrate the appearance of the modulation, we sketch one spiral arm and two circles in Fig. 5(e). At a given radius the spiral arm crosses a circle at a specific angle, in Fig. 5(e) at 270° for the smaller circle (yellow point) and at 180° for the larger circle (red point). The yield at these angles is different, due to the dipolar pattern. We obtain a higher yield at electron energies corresponding to radii, for which the circle cosses the spiral on the p_x

axis in the PMD, where the dipolar pattern maximizes. The rotation of the spiral as a function of the nuclear energy, see Fig. 2, leads to a linear shift of the crossing angle and thus, to the correlation lines in the JES. Note that the PMDs exhibit two spiral arms rotated by an angle of π relative to each other. This matches the π-periodic structure of the dipolar pattern, so that both spiral arms produce the same correlation pattern in the JES.

In Fig. 5(d) we compare of the electron-energy spectrum for the fixed-nuclei simulation, for the atom, and the JES Fig. 5(b) integrated over all shown nuclear energies. In case of the atom, the spiral interference structure does not show any dipolar pattern, see Fig. 3(d), so the energy spectrum is a smooth curve similar to the energy spectrum for a single pulse. The fixed-nuclei simulation and the full coupled TDSE result show a modulation with distinct maxima and minima. The yellow and red points serve as references for the two exemplary radii in Fig. 5(e), which correspond to a yield minimum and maximum within the dipolar pattern for fixed nuclei. More complicated dynamical FEVs of molecules, see for example for CO or HF in [27], might lead to other structures than equidistant peaks. The difference between fixed-nuclei and moving-nuclei results in Fig. 5(d) is caused again by integrating over different vibrational states.

Last, we mention some additional aspects not shown in this article. When the alignment angle of the molecule is changed, the dipolar pattern rotates accordingly, but the spiral (slope and rotation angle) stays the same. The resulting horizontal shift of the correlation lines in Fig. 5(b) implies that for randomly oriented molecules the modulation in the JES and in the electron-energy spectrum might average out, leading to an atom-like result. This does not apply to the RRCP setup, which shows the correlation lines regardless of the dipolar pattern. Similarly, averaging over orientations may wash out the dipolar pattern of Fig. 3(b), but the blurred spiral should persist.

IV. CONCLUSION

In this article we have demonstrated a quantum-mechanical calculation of free-electron vortices for coupled electronic-nuclear motion. We have shown that the spiral interference obtained in the PMD from one-photon single ionization of aligned H_2 with a counter-rotating pulse pair rotates as a function of the energy of the nuclei. The rotation can be described very accurately by a kinetic formula assuming instantaneous energy sharing between photoelectron and nuclei. The rotation is washed out when the measurement includes integration over the nuclear energy. Thus, although the interference is still visible for the $H_2^+ + e^-$ channel integrated over all vibrational bound states, the rotation angle of the spiral differs notably from any specific vibrational state. Additionally, we have compared our moving-nuclei results to a fixed-nuclei simulation showing that the general shape is well reproduced, but the rotation agrees only if a single vibrational state of the moving-nuclei photoion is considered such that the ionization potential is similar to the fixed-nuclei case. For the dissociation channel we have shown an increasing shift of the rotation angle as a function of the integration range of the kinetic-energy release. We have demonstrated the appearance of correlation lines in the joint-energy spectrum. These lines are caused by the dipolar pattern in the photoelectron momentum distributions, which originates from the non-isotropic shape of the molecular orbital undergoing ionization.

The reported rotation of the vortices can be used to gauge the time-delay τ, gain information about the energy sharing process, or extract properties of dynamical FEVs. The relative carrier-envelope phase ϕ_{12} has a similar effect, i.e., rotation in the polarization plane. The induced correlation between electron and nuclei may provide a new tool for controlled nuclear dynamics. Future projects may apply the developed TDSE model to other settings such as tunnel ionization, different field polarizations, e.g., "bicircular" polarization [16, 52], or longer pulses with significant nuclear motion during ionization. For a recent application of the model to entangled electron–nuclear dynamics, see [53]. Furthermore, certain phenomena in the creation of free-electron vortices – such as the synchronization of the pulse sequence with nuclear motion – have been previously described using semiclassical models but still require validation through a full quantum-mechanical treatment [28].

ACKNOWLEDGMENTS

This work was funded by the Deutsche Forschungsgemeinschaft (DFG, German Research Foundation) through the project 498967973. Numerical simulations were mostly performed on compute clusters at the Leibniz University Hannover, which were funded by the Deutsche Forschungsgemeinschaft (DFG, German Research Foundation) under project numbers 411116428, 424969120, and 563020064.

Appendix A: Notes on the non-Born-Oppenheimer model

In this section we elaborate on the non-BO TDSE model and provide numerical details to ensure reproducibility. In addition, we discuss prospects for improving the model.

We start with the full Hamiltonian of the 4 particles with masses m_k, charges q_k and positions $\vec{x}_k$ with $k = \{1,2\}$ for the nuclei and $k = \{3,4\}$ for the electrons,

$$\begin{aligned} H =& T_{e_1} + T_{e_2} + T_{\mathrm{nuc}} + \\ & V_{e_1e_2} + V_{e_1,\mathrm{nuc}} + V_{e_2,\mathrm{nuc}} + V_{\mathrm{nuc}} + \\ & H_{\mathrm{int}}(t)\,, \end{aligned} \tag{A1}$$

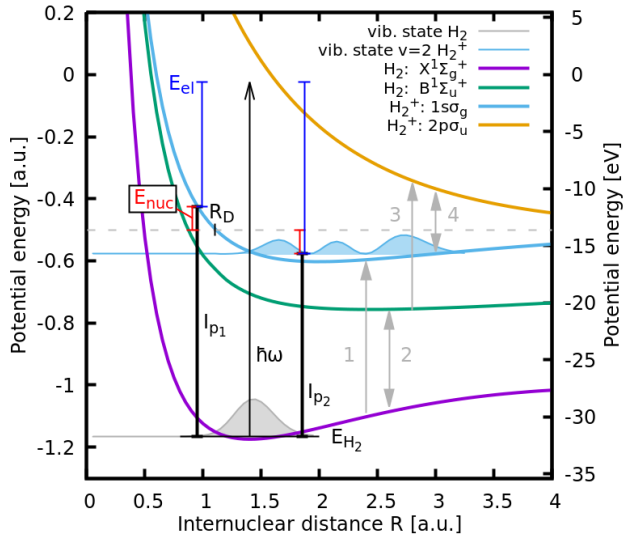

Figure A1. Energy potential curves of H_2 and H_2^+ used in the model. The large arrow labeled $\hbar\omega$ shows the photon energy. Numbered arrows (1-4) illustrate different mechanisms how population can be transferred between the states: (1) and (3) by removing the active electron $|\vec{r}| \to \infty$, (2) and (4) by population transfer in the two-level system driven by the interaction potential $W = -\vec{d}(\vec{r}, R) \cdot \vec{\mathcal{E}}(t)$. Vertical lines labeled E_{nuc}, E_{el}, $I_{p_1} = I_p^{\mathrm{vert}}(R = 0.95\,\mathrm{a.u.})$, and $I_{p_2} = I_p^{\mathrm{adi}}(v = 3)$ illustrate two examples of the described energy sharing Eq. (4) with neglected ponderomotive potential U_p.

where the T's contain the kinetic energies of each electron and each nuclei, $V_{e_1e_2}$ is the repulsive electron-electron interaction, $V_{e_1,\mathrm{nuc}}$ and $V_{e_2,\mathrm{nuc}}$ are the attractive electron-nuclei interactions, V_{nuc} is the repulsive nuclear-nuclear interaction, and $H_{\mathrm{int}}(t)$ the time-dependent interaction with the laser field. We pursue two avenues of simplification: (i) physically motivated modifications of the Hamiltonian reducing the complexity and (ii) a separation ansatz for the wave function distinguishing between an active electron, which can be ejected, and an inactive electron, which is assumed to stays always bound.

First, we perform a coordinate transformation into the Jacobi coordinates

$$\vec{R}_{\mathrm{COM}} = \sum_{k=1}^{4} \frac{m_k \vec{x}_k}{M_4} \tag{A2}$$

$$\vec{R} = \vec{x}_1 - \vec{x}_2 \tag{A3}$$

$$\vec{r}_1 = \vec{x}_3 - \frac{m_1\vec{x}_1 + m_2\vec{x}_2}{M_2} \tag{A4}$$

$$\vec{r}_2 = \vec{x}_4 - \frac{\sum_{k=1}^{3} m_k \vec{x}_k}{M_3} \tag{A5}$$

with $M_l = \sum_{k=1}^{l} m_k$. We drop the center-of-mass motion and assume the rotation of the molecule to be negligible. This reduces the dimensionality from 12 to 7. We set the reduced masses appearing in the transformed kinetic energy terms of the electrons to one, which is justified by the large difference in mass between electrons and nuclei, $m_e \ll M_2$. The interaction of the external electric field with the internuclear distance $R = |\vec{R}|$ vanishes for H_2, because the nuclei have identical masses and charges. The interaction with the electric field reads in Jacobi coordinates

$$H_{\mathrm{int}} = (-\vec{x}_1 - \vec{x}_2 + \vec{x}_3 + \vec{x}_4) \cdot \vec{\mathcal{E}}(t) = (\kappa\vec{r}_1 + \vec{r}_2) \cdot \vec{\mathcal{E}}(t)\,, \tag{A6}$$

with $\kappa = M_4/M_3 = 2(m_e + m_{\mathrm{H}^+})/(2m_{\mathrm{H}^+} + m_e)$, the charges $q_1 = q_2 = -q_3 = -q_4 = 1$ and the masses $m_1 = m_2 = m_{\mathrm{H}^+}$ and $m_3 = m_4 = m_e$.

Next, we introduce the distinction between active and inactive electron. We assign $\vec{r}_1$ to the inactive electron and $\vec{r}_2$ to the active electron (equivalent to $\vec{r}$ in the main text). The total wave function is expanded in time-independent functions $\phi_j(\vec{r}_1; \vec{r}_2, R)$, which describe the inactive electron's wave function, parametrically dependent on the active electron's coordinate and the internuclear distance, for the jth state, and time-dependent functions $\psi_j(\vec{r}_2, R, t)$,

$$\Psi(\vec{r}_1, \vec{r}_2, R; t) = \sum_{j=0}^{\infty} \phi_j(\vec{r}_1; \vec{r}_2, R)\psi_j(\vec{r}_2, R, t)\,. \tag{A7}$$

The time-independent part ϕ_j should fulfill the one-particle Schrödinger equation

$$H_{e_1}\phi_j(\vec{r}_1; \vec{r}_2, R) = E_j^{\mathrm{eff}}(\vec{r}_2, R)\phi_j(\vec{r}_1; \vec{r}_2, R) \tag{A8}$$

with

$$H_{e_1} = T_{e_1} + V_{e_1e_2} + V_{e_1,\mathrm{nuc}} + V_{\mathrm{nuc}} + V_{e_2,\mathrm{nuc}}\,. \tag{A9}$$

This yields an effective interaction potential $E_j^{\mathrm{eff}}(\vec{r}_2, R)$ between the active electron and the nuclei for each energy level j of the inactive electron. Up to this point, the expansion is exact. Inserting the expansion into the TDSE, $i\partial\Psi = H\Psi$, and projecting onto an arbitrary inactive-electron state ϕ_m yields a matrix–vector form of the TDSE. As in the original Born–Oppenheimer ansatz [54], where the time-independent part ϕ_j contains all electronic coordinates and the time-dependent part describes only nuclear motion, we obtain nonadiabatic coupling terms, i.e., derivatives of ϕ_j with respect to the active-electron and nuclear coordinates arising from the kinetic-energy operator. Whereas in the standard BO ansatz the nonadiabatic couplings scale with the inverse reduced nuclear mass and are usually small, our formulation includes electron–electron interactions in both diagonal and off-diagonal matrix elements, which can be substantial. Nonetheless, we neglect all nonadiabatic couplings. Instead of solving Eq. (A8) to obtain the potential-energy surface $E_j^{\mathrm{eff}}(\vec{r}_2, R)$, we model the interaction with soft-core potentials Eq. (6) and the BO potential curves of the ion,

$$E_j^{\mathrm{eff}}(\vec{r}_2, R) \approx V_j^{\mathrm{int}}(\vec{r}_2, R) + V_j^{\mathrm{ion}}(R)\,. \tag{A10}$$

Bypassing Eq. (A8) reduces the computational load dramatically and allows us to approximately correct for the missing diagonal coupling terms of the electron-electron interaction. The BO potential curve V_j^{ion} ensures the correct energies of the ion when the active electron is far away and the soft-core potential $V_j^{\mathrm{int}}(\vec{r}_2, R)$ fixes the correct ionization potential. However, the model misses off-diagonal electron-electron interaction, which would be relevant for excitation of the inactive electron in recollision events needed for example in high-order above-threshold dissociation [38].

We restrict the sum in Eq. (A7) to only two terms as a compromise between required computational resources and accurate description of H_2 and H_2^+. Two levels are sufficient to model a variety of effects including bond-softening and bond-hardening [34, 35, 55], above-threshold dissociation [37], and electron localization [36]. As we invoke the dipole approximation and we use only planar field polarizations, we restrict the coordinate of the active electron to two dimensions $\vec{r}_2 = (x, y)^T$. The two-level three-dimensional TDSE reads

$$\mathrm{i}\partial_t \begin{pmatrix} \psi_0(\vec{r}_2, R) \\ \psi_1(\vec{r}_2, R) \end{pmatrix} = \begin{pmatrix} H_0 & W \\ W & H_1 \end{pmatrix} \begin{pmatrix} \psi_0(\vec{r}_2, R) \\ \psi_1(\vec{r}_2, R) \end{pmatrix}, \quad \text{(A11)}$$

with $W = \langle \phi_1 | H_{\mathrm{int}}(t) | \phi_0 \rangle_{(\vec{r}_1)} = -\vec{d}(\vec{r}_2, R) \cdot \vec{\mathcal{E}}(t)$. We transformed the interaction term, $\vec{r}_2 \cdot \vec{\mathcal{E}}$, from the length gauge to the velocity gauge to arrive at Eq. (7). The active electron is not restricted to a certain number of states. It can populate all intermediate states and continuum states after ionization, as long as they are numerically available on the grid. This method is an improved single-active electron approach with coupled electron-nuclear motion, hence, beyond the standard BO approximation. The effective charge and the softening parameter are defined similar to [56] as

$$Z_j^{\mathrm{eff}}(R, |\vec{u}_k|) = \frac{1}{2}\left(1 + z_j \mathrm{e}^{-\frac{|\vec{u}_k|^2}{\sigma_j(R)^2}}\right), \quad \text{(A12)}$$

$$\alpha_j(R) = \delta_{j1} R + \frac{1}{2}, \quad \text{(A13)}$$

where $\delta_{j1} = 1$ is a Kronecker delta and $\vec{u}_k = \vec{r}_2 - \vec{R}_k$ with $k = \{1, 2\}$. Equations (A12) and (A13) model the screening of the nuclei by the inactive electron. The constant parameters are given by $z_0 = 1$ and $z_1 = 2$. The limits of the effective charges are $Z_j^{\mathrm{eff}}(|\vec{u}| \to 0) = \{1, 3/2\}$ for $j = \{0, 1\}$ and $Z_j^{\mathrm{eff}}(|\vec{u}| \to \infty) = 1/2$ for both j. We had to increase the effective charge for the second level ($j = 1$) beyond the physically motivated charge of 1 to numerically reach the correct ionization potential $\Delta V_1(R)$ for all R in combination with an R-dependent softening parameter to stabilize the optimization procedure and keep all parameters in a reasonable definition range. We applied the Newton–Raphson method [57] with imaginary-time propagation and the real-time propagator eigenstate method [47, 48] for the fixed-nuclei two-dimensional TDSE

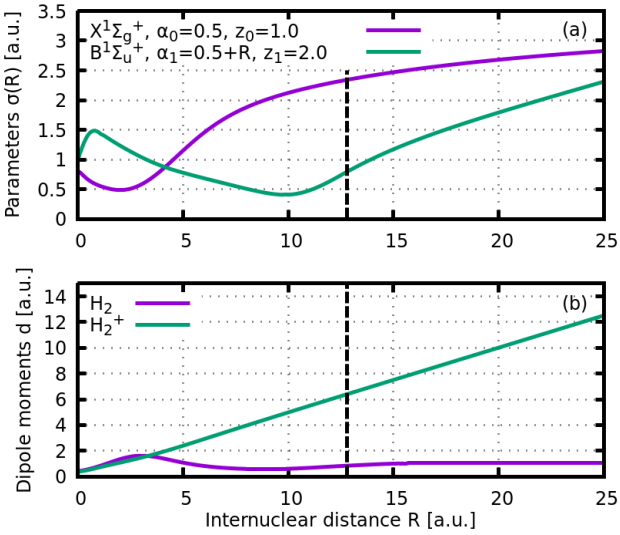

Figure A2. (a) Optimized parameters $\sigma_j(R)$ for both states of H_2. (b) Transition dipole moments between the lowest two dipole-allowed electronic states of H_2 and H_2^+ as a function of the internuclear distance, obtained from the literature [58–61].

$$H_{e_2}(\sigma_j)\psi_j(\vec{r}_2) = -\Delta V_j(R)\psi_j(\vec{r}_2), \quad \text{(A14)}$$

with

$$H_{e_2} = T_{e_2} + V_j^{\mathrm{int}}(\vec{r}_2, R), \quad \text{(A15)}$$

to search for $\sigma_j(R)$ leading to the correct ionization potential $\Delta V_j(R) = V_j^{\mathrm{ion}}(R) - V_j^{\mathrm{H_2}}(R)$ for both states of H_2. Thus, the parameter $\sigma_j(R)$ in the interaction potential V_j^{int} fixes only the ground-state energy of the active electron, which depends on the state j of the second electron. The optimized parameters are given in Fig. A2(a). Excited states of the active electron deviate from literature values and do not exhibit the correct R-dependence. For instance, the first excited state of the active electron dissociates to the same asymptotic energy as the ground state. This happens because the interaction potential $V_j^{\mathrm{int}}(\vec{r}_2, R)$ is symmetric with respect to $\vec{r}_2$ along the molecular axis. Nevertheless, we expect this incorrect behavior to not influence the results much, because the ionization is fast compared to the nuclear motion.

We show the used BO potential curves $V_j^{\mathrm{ion}}(R)$ and $V_j^{\mathrm{H_2}}(R)$ for $j = \{0, 1\}$ in Fig. A1. These are obtained by analytical approximations from [39] for the H_2 ground state and the H_2^+ ground and excited states. The dipole-allowed excited state of H_2 ($B^1\Sigma_u^+$) is taken from [40, 41]. To adjust the provided curve to the used R grid, we extrapolated the data for small R as $E_{\mathrm{He},1} + 1/R + a_1 R + a_2 R^2$ with $E_{\mathrm{He},1}$ the first excited state of He [42] and for large R as $-0.625 - \sum_{k=5}^{8} a_k / R^k$ leading to a sufficiently smooth curve. The a-parameters

are obtained by fitting the extrapolation functions to a few of the outer points from the provided data. The gray arrows numbered 1-4 in Fig. A1 illustrate the possibilities how population can be transferred between the states within this model. First, both up-arrows 1 and 3 illustrate the ionization process when $|\vec{r}_2| \to \infty$ and the interaction potential vanishes, $V_j^{\mathrm{int}}(|\vec{r}_2| \to \infty, R) \to 0$. This process is nonreversible for two reasons. First, when the electron is removed by a circularly polarized pulse, it will not come back. Second, the two-grid method prevents an absorbed electron wave packet to return to the parent ion. In process 2 and 4, which can go in both directions, population is transferred by the electric field via the interaction potential W of the two-level Hamiltonian Eq. (9). The dipole moment differs between H_2 and H_2^+. Because the ϕ_j's from Eq. (A7) are not available to us, we decide to model this transition using a three-dimensional function

$$\vec{d}(\vec{r}_2, R) = f(u_1, u_2)\vec{d}_{\mathrm{H_2}}(R) + [1 - f(u_1, u_2)]\,\vec{d}_{\mathrm{H_2^+}}(R) \tag{A16}$$

with $u_k = |\vec{r}_2 - \vec{R}_k|$ and $k = \{1, 2\}$, and we set $\kappa = 1$. We assume $\hat{e}_y \parallel \vec{d}_{\mathrm{H_2}}(R) \parallel \vec{d}_{\mathrm{H_2^+}}(R)$, motivated by the symmetry of the states, with $|\vec{d}_{\mathrm{H_2}}(R)|$ and $|\vec{d}_{\mathrm{H_2^+}}(R)|$ given in Fig. A2(b), taken from the literature [58–61]. The transition area is a combined region of two circles around each nucleus. The transition function is given by

$$f(u_1, u_2) = \max\left[g(u_1), g(u_2)\right] \tag{A17}$$

$$\text{with} \qquad g(u) = \mathrm{e}^{-\frac{u}{3}}\,. \tag{A18}$$

Within the two-grid method, the dipole moment reduces to $\vec{d}_{\mathrm{H_2^+}}(R)$ in the outer region. We expect this model to be physically reasonable as long as the ionization proceeds at comparable small internuclear distances.

To improve the model, explicit electron-electron interactions could be introduced in the off-diagonal matrix elements of Eq. (A11). When necessary, more than two levels could be used. Further, one could check whether Eq. (A10) holds, by estimating the ϕ_j functions based on quantum-chemistry calculations. In this way, also a better approximation of the dipole interaction Eq. (A16) could be found.

Last, we want to summarize the introduced molecular ionization potentials. The difference between BO potential curves,

$$I_p = \Delta V_j(R) = V_j^{\mathrm{ion}}(R) - V_j^{\mathrm{H_2}}(R)\,, \tag{A19}$$

is used in fixed-nuclei simulations and for finding the parameters of the soft-core potentials. In contrast, in the moving-nuclei simulations, the energy of the nuclei has to be considered as a part of the energy conservation. For the direct dissociation channel, we assume ionization of the molecule at small internuclear distances $R < R_D$ with the vertical ionization potential

$$I_p = I_p^{\mathrm{vert}}(R) = V_0^{\mathrm{ion}}(R) - E_{\mathrm{H_2}}\,. \tag{A20}$$

When the molecular ion ends up in a vibrational bound state, i.e., for ionization at larger internuclear distances $R > R_D$, we use a generalized adiabatic ionization potential

$$I_p = I_p^{\mathrm{adi}}(v) = E_{0,v} - E_{\mathrm{H_2}}\,. \tag{A21}$$

With the definitions of E_{nuc}, see main text, we end up in both cases with the expression

$$I_p = E_{\mathrm{nuc}} + V_D - E_{\mathrm{H_2}}\,. \tag{A22}$$

Figure A1 shows two examples for the energy conservation Eq. (4) with the nuclear energy E_{nuc} as red vertical lines, the energy of the electron E_{el} as blue vertical lines, and the ionization potentials as thick black vertical lines in comparison to the black vertical arrow indicating the photon energy $\hbar\omega$. When the internuclear distance is smaller than R_D, the nuclear energy is continuous and positive. Potential energy is built up in the ionization process and released by motion along the ion's potential curve. Thus, the energy needed to ionize (ionization potential) is partially converted into kinetic energy of the nuclei. The ionization potential is the difference between the initial vibrational state and the ion's BO potential curve. When the internuclear distance is larger than R_D, the nuclear energy is negative and the molecular ionization potential is the difference between the initial and final vibrational state.

[1] P.-L. He, N. Takemoto, and F. He, Photoelectron momentum distributions of atomic and molecular systems in strong circularly or elliptically polarized laser fields, Phys. Rev. A **91**, 063413 (2015).

[2] A. Bunjac, D. B. Popović, and N. S. Simonović, Calculations of photoelectron momentum distributions and energy spectra at strong-field multiphoton ionization of sodium, The European Physical Journal D **71**, 208 (2017).

[3] N. Douguet and K. Bartschat, Photoelectron momentum distributions in the strong-field ionization of atomic hydrogen by few-cycle elliptically polarized optical pulses, Phys. Rev. A **106**, 053112 (2022).

[4] P. Eckle, M. Smolarski, P. Schlup, J. Biegert, A. Staudte, M. Schöffler, H. G. Muller, R. Dörner, and U. Keller, Attosecond angular streaking, Nat. Phys. **4**, 565 (2008).

[5] L. Torlina, F. Morales, J. Kaushal, I. Ivanov, A. Kheifets, A. Zielinski, A. Scrinzi, H. G. Muller, S. Sukiasyan,

M. Ivanov, and O. Smirnova, Interpreting attoclock measurements of tunnelling times, Nat. Phys. **11**, 503 (2015).
[6] D. Trabert, N. Anders, A. Geyer, M. Hofmann, M. S. Schöffler, L. P. H. Schmidt, T. Jahnke, M. Kunitski, R. Dörner, and S. Eckart, Angular dependence of the Wigner time delay upon strong-field ionization from an aligned p orbital, Phys. Rev. Res. **5**, 023118 (2023).
[7] T. Zuo, A. Bandrauk, and P. Corkum, Laser-induced electron diffraction: a new tool for probing ultrafast molecular dynamics, Chem. Phys. Lett. **259**, 313 (1996).
[8] M. Lein, J. P. Marangos, and P. L. Knight, Electron diffraction in above-threshold ionization of molecules, Phys. Rev. A **66**, 051404 (2002).
[9] M. Meckel, D. Comtois, D. Zeidler, A. Staudte, D. Pavičić, H. C. Bandulet, H. Pépin, J. C. Kieffer, R. Dörner, D. M. Villeneuve, and P. B. Corkum, Laser-induced electron tunneling and diffraction, Science **320**, 1478 (2008).
[10] C. I. Blaga, J. Xu, A. D. DiChiara, E. Sistrunk, K. Zhang, P. Agostini, T. A. Miller, L. F. DiMauro, and C. D. Lin, Imaging ultrafast molecular dynamics with laser-induced electron diffraction, Nature **483**, 194 (2012).
[11] B. Belsa, K. M. Ziems, A. Sanchez, K. Chirvi, X. Liu, S. Gräfe, and J. Biegert, Laser-induced electron diffraction in the over-the-barrier-ionization regime, Phys. Rev. A **106**, 043105 (2022).
[12] Y. Huismans, A. Rouzée, A. Gijsbertsen, J. H. Jungmann, A. S. Smolkowska, P. S. W. M. Logman, F. Lépine, C. Cauchy, S. Zamith, T. Marchenko, J. M. Bakker, G. Berden, B. Redlich, A. F. G. van der Meer, H. G. Muller, W. Vermin, K. J. Schafer, M. Spanner, M. Y. Ivanov, O. Smirnova, D. Bauer, S. V. Popruzhenko, and M. J. J. Vrakking, Time-Resolved Holography with Photoelectrons, Science **331**, 61 (2011).
[13] S. G. Walt, N. Bhargava Ram, M. Atala, N. I. Shvetsov-Shilovski, A. von Conta, D. Baykusheva, M. Lein, and H. J. Wörner, Dynamics of valence-shell electrons and nuclei probed by strong-field holography and rescattering, Nat. Commun. **8**, 15651 (2017).
[14] C. Figueira de Morisson Faria and A. S. Maxwell, It is all about phases: ultrafast holographic photoelectron imaging, Rep. Prog. Phys. **83**, 034401 (2020).
[15] S. Brennecke, N. Eicke, and M. Lein, Gouy's phase anomaly in electron waves produced by strong-field ionization, Phys. Rev. Lett. **124**, 153202 (2020).
[16] P. Winter and M. Lein, Bicircular attoclock with molecules as a probe of strong-field stark shifts and molecular properties, Phys. Rev. A **109**, L020801 (2024).
[17] J. M. Ngoko Djiokap, S. X. Hu, L. B. Madsen, N. L. Manakov, A. V. Meremianin, and A. F. Starace, Electron vortices in photoionization by circularly polarized attosecond pulses, Phys. Rev. Lett. **115**, 113004 (2015).
[18] D. Pengel, S. Kerbstadt, D. Johannmeyer, L. Englert, T. Bayer, and M. Wollenhaupt, Electron vortices in femtosecond multiphoton ionization, Phys. Rev. Lett. **118**, 053003 (2017).
[19] K.-J. Yuan, S. Chelkowski, and A. D. Bandrauk, Photoelectron momentum distributions of molecules in bichromatic circularly polarized attosecond UV laser fields, Phys. Rev. A **93**, 053425 (2016).
[20] J. M. Ngoko Djiokap, A. V. Meremianin, N. L. Manakov, S. X. Hu, L. B. Madsen, and A. F. Starace, Multistart spiral electron vortices in ionization by circularly polarized UV pulses, Phys. Rev. A **94**, 013408 (2016).
[21] J. M. N. Djiokap, A. V. Meremianin, N. L. Manakov, S. X. Hu, L. B. Madsen, and A. F. Starace, Kinematical vortices in double photoionization of helium by attosecond pulses, Phys. Rev. A **96**, 013405 (2017).
[22] J. M. Ngoko Djiokap, A. V. Meremianin, N. L. Manakov, L. B. Madsen, S. X. Hu, and A. F. Starace, Dynamical electron vortices in attosecond double photoionization of H_2, Phys. Rev. A **98**, 063407 (2018).
[23] D. Pengel, S. Kerbstadt, L. Englert, T. Bayer, and M. Wollenhaupt, Control of three-dimensional electron vortices from femtosecond multiphoton ionization, Phys. Rev. A **96**, 043426 (2017).
[24] T. Bayer, C. Philipp, K. Eickhoff, and M. Wollenhaupt, Atomic photoionization dynamics in ultrashort cycloidal laser fields, Phys. Rev. A **102**, 013104 (2020).
[25] R.-R. Wang, M.-Y. Ma, L.-C. Wen, Z. Guan, Z.-Q. Yang, Z.-H. Jiao, G.-L. Wang, and S.-F. Zhao, Comparative study of electron vortices in photoionization of molecules and atoms by counter-rotating circularly polarized laser pulses, J. Opt. Soc. Am. B **40**, 1749 (2023).
[26] S. Kerbstadt, K. Eickhoff, T. Bayer, and M. Wollenhaupt, Odd electron wave packets from cycloidal ultrashort laser fields, Nat. Commun. **10**, 658 (2019).
[27] H. B. Ambalampitiya and J. M. Ngoko Djiokap, Orientation-dependent production of normal archimedean and dynamical spirals for revealing orbital symmetries in diatomic multi-orbital molecules, Commun. Phys. **7**, 359 (2024).
[28] T. Bayer and M. Wollenhaupt, Molecular free electron vortices in photoionization by polarization-tailored ultrashort laser pulses, Front. Chem. **10**, 899461 (2022).
[29] X. Kong, G. Zhang, M. Li, T. Wang, X. Ding, and J. Yao, Odd-fold-symmetric spiral momentum distributions and their stark distortions in hydrogen, J. Opt. Soc. Am. B **35**, 2163 (2018).
[30] M. Li, G. Zhang, X. Ding, and J. Yao, AC stark effect on vortex spectra generated by circularly polarized pulses, IEEE Photonics J. **11**, 1 (2019).
[31] Y.-N. Qin, M. Li, Y. Feng, S. Luo, Y. Zhou, and P. Lu, Extracting the phase distribution of the electron wave packet ionized by an elliptically polarized laser pulse, Front. Phys. **16**, 32502 (2020).
[32] J. M. N. Djiokap and A. F. Starace, Doubly-excited state effects on two-photon double ionization of helium by time-delayed, oppositely circularly-polarized attosecond pulses, J. Opt. **19**, 124003 (2017).
[33] J. M. Ngoko Djiokap and A. F. Starace, Temporal coherent control of resonant two-photon double ionization of the hydrogen molecule via doubly excited states, Phys. Rev. A **103**, 053110 (2021).
[34] P. H. Bucksbaum, A. Zavriyev, H. G. Muller, and D. W. Schumacher, Softening of the H_2^+ molecular bond in intense laser fields, Phys. Rev. Lett. **64**, 1883 (1990).
[35] L. J. Frasinski, J. H. Posthumus, J. Plumridge, K. Codling, P. F. Taday, and A. J. Langley, Manipulation of bond hardening in H_2^+ by chirping of intense femtosecond laser pulses, Phys. Rev. Lett. **83**, 3625 (1999).
[36] H. Xu, Z. Li, F. He, X. Wang, A. Atia-Tul-Noor, D. Kielpinski, R. T. Sang, and I. V. Litvinyuk, Observing electron localization in a dissociating H_2^+ molecule in real time, Nat. Commun. **8**, 15849 (2017).
[37] A. Giusti-Suzor, X. He, O. Atabek, and F. H. Mies, Above-threshold dissociation of H_2^+ in intense laser fields, Phys. Rev. Lett. **64**, 515 (1990).

[38] P. Lu, J. Wang, H. Li, K. Lin, X. Gong, Q. Song, Q. Ji, W. Zhang, J. Ma, H. Li, H. Zeng, F. He, and J. Wu, High-order above-threshold dissociation of molecules, Proc. Natl. Acad. Sci. U.S.A. **115**, 2049 (2018).

[39] H. Olivares-Pilón and A. V. Turbiner, H_2^+, HeH and H_2: Approximating potential curves, calculating rovibrational states, Ann. Phys. **393**, 335 (2018).

[40] M. Siłkowski, M. Zientkiewicz, and K. Pachucki, Accurate Born-Oppenheimer potentials for excited σ^+ states of the hydrogen molecule, in *New Electron Correlation Methods and their Applications, and Use of Atomic Orbitals with Exponential Asymptotes* (Elsevier, 2021) p. 255–267.

[41] K. Pachucki and M. Silkowski, Personal communication (2024), Data for $1^1\Sigma_u^+$ in https://arxiv.org/src/2104.03174v2/anc/supp.txt have misprints but are corrected in the PhD thesis of Michal Silkowski.

[42] D. T. Aznabayev, A. K. Bekbaev, I. S. Ishmukhamedov, and V. I. Korobov, Energy levels of a helium atom, Phys. Part. Nuclei Lett. **12**, 689 (2015).

[43] P. J. Mohr, D. B. Newell, B. N. Taylor, and E. Tiesinga, CODATA recommended values of the fundamental physical constants: 2022, Rev. Mod. Phys. **97**, 025002 (2025), proton Mass; available online from `https://physics.nist.gov/cgi-bin/cuu/Value?mp` accessed: 2024-08.

[44] M. Feit, J. Fleck, and A. Steiger, Solution of the Schrödinger equation by a spectral method, J. Comp. Phys. **47**, 412 (1982).

[45] F. Oppermann, The HeH^+ Isotopologues in Intense Asymmetric Laser Fields, Ph.D. thesis, Gottfried Willhelm Leibniz Unitersity Hannover (2023).

[46] M. Lein, E. K. U. Gross, and V. Engel, Intense-Field Double Ionization of Helium: Identifying the Mechanism, Phys. Rev. Lett. **85**, 4707 (2000).

[47] R. Kosloff and H. Tal-Ezer, A direct relaxation method for calculating eigenfunctions and eigenvalues of the schrödinger equation on a grid, Chem. Phys. Lett. **127**, 223 (1986).

[48] F. Oppermann, N. Eicke, and M. Lein, Real-time propagator eigenstates, J. Phys. B: At. Mol. Opt. Phys. **55**, 19LT01 (2022).

[49] S. A. Alexander and R. L. Coldwell, Vibrational–rotational energies of all H_2 isotopomers using monte carlo methods, Int. J. Quantum Chem. **106**, 1820 (2006).

[50] P. Billaud, M. Géléoc, Y. J. Picard, K. Veyrinas, J. F. Hergott, S. Marggi Poullain, P. Breger, T. Ruchon, M. Roulliay, F. Delmotte, F. Lepetit, A. Huetz, B. Carré, and D. Dowek, Molecular frame photoemission in dissociative ionization of H_2 and D_2 induced by high harmonic generation femtosecond XUV pulses, J. Phys. B: At. Mol. Opt. Phys. **45**, 194013 (2012).

[51] We must change the fitting procedure from finding maxima along circles to maxima along radial cuts, because the dipolar pattern leads to maxima on the p_x axis for all radii.

[52] N. Eicke, S. Brennecke, and M. Lein, Attosecond-Scale Streaking Methods for Strong-Field Ionization by Tailored Fields, Phys. Rev. Lett. **124**, 043202 (2020).

[53] S. Hell, P. Winter, M. Gärttner, J. Späthe, S. Mhatre, D. B. Milošević, G. G. Paulus, M. Lein, and M. Kübel, Entanglement and photoelectron holography in dissociative photoionization: molecular quantum eraser, arXiv:2604.16107 (2026).

[54] A. Szabo and N. S. Ostlund, *Modern Quantum Chemistry: Introduction to Advanced Electronic Structure Theory* (McGraw–Hill, New York, 1982).

[55] A. Giusti-Suzor and F. H. Mies, Vibrational trapping and suppression of dissociation in intense laser fields, Phys. Rev. Lett. **68**, 3869 (1992).

[56] M. Lein, Attosecond probing of vibrational dynamics with high-harmonic generation, Phys. Rev. Lett. **94**, 053004 (2005).

[57] W. H. Press, S. A. Teukolsky, W. T. Vetterling, and B. P. Flannery, *Numerical Recipes: The Art of Scientific Computing*, 3rd ed. (Cambridge University Press, Cambridge, UK, 2007).

[58] T. Tsogbayar and T. Banzragch, The oscillator strengths of H_2^+, $1s\sigma_g$-$2p\sigma_u$, $1s\sigma_g$-$2p\pi_u$, arXiv:1007.4354 (2010).

[59] D. E. Ramaker and J. M. Peek, Dipole strengths involving the lowest twenty electronic states of H_2^+, At. Data Nucl. Data Tables **5**, 167 (1973).

[60] D. R. Bates, The oscillator strength of H_2^+, $1s\sigma$—$2p\sigma$, J. Chem. Phys. **19**, 1122 (1951).

[61] L. Wolniewicz and G. Staszewska, $1\sigma_u^+ \rightarrow X^1\sigma_g^+$ transition moments for the hydrogen molecule, J. Mol. Spectrosc. **217**, 181 (2003).